

Particle selection from an equilibrium DF

J. A. Sellwood*

Steward Observatory, University of Arizona, 933 N Cherry Ave, Tucson AZ 85722, USA

1 March 2024

ABSTRACT

When starting an N -body simulation of an isolated galaxy, it is desirable to select particles from a distribution function to ensure that the model is in equilibrium. Random sampling from a DF is widely used, but results in a set of particles that differs by shot noise from that intended. This paper presents a method to reduce sampling noise that has been developed by the author in a many collaborations over a number of years. The technique has been partly described in past papers, though the ideas have not previously been gathered together, nor have its advantages been clearly demonstrated in past work. Of course, sampling errors can also be reduced by a brute force increase in the number of particles, but methods to achieve the same effect with fewer particles have obvious advantages. Here we not only describe the method, but also present three sets of simulations to illustrate the practical advantages of reducing sampling error. The improvements are not dramatic, but are clearly worth having.

Key words: galaxies: general — galaxies: kinematics and dynamics — methods: numerical

1 INTRODUCTION

Our understanding of the dynamics of isolated model galaxies has been considerably advanced by N -body simulation, particularly of models that begin from a settled state. Yet creating an equilibrium set of particles from which to start remains one of the most challenging steps. The simplest models are single component disks or spheroids in which all the mass is in the particles, but one may wish to embed the self-gravitating particles in an externally imposed, rigid gravitational field or, in more elaborate models, to represent the disk, bulge and halo as separate components in a combined equilibrium model. Note that the gravitational potential in any model is the total arising from all mass components, whether rigid or composed of mobile particles, but the distribution function (DF) for each component must be an equilibrium function in the total potential.

Sellwood & Athanassoula (1986), Hernquist (1993), Kuijken & Dubinski (1995), Debattista & Sellwood (2000), Holley-Bockelmann, Weinberg & Katz (2005), Widrow *et al.* (2008), Rodionov, Athanassoula & Sotnikova (2009), Yurin & Springel (2014), and others have offered techniques to create single or multi-component models, which achieve something increasingly close to a global equilibrium. Perhaps the most sophisticated are the AGAMA models by Vasiliev (2019), who uses iterative techniques to devise equilibrium distribution functions (DFs) for each component in the combined potential. The DF is generally expressed as a function of integrals $\{\mathbf{I}\}$, such as the classical energy and angular momentum $f(E, \mathbf{L})$ or actions $f(\mathbf{J})$.

However, having found an equilibrium DF, many practi-

tioners simply select N particles at random from the DF. The procedure is to generate candidate particles that are uniformly distributed in each dimension of (\mathbf{x}, \mathbf{v}) -space, and then select only those for which $f(\mathbf{I}) > tf_{\max}$, with t being a random value from a uniform distribution $0 \leq t \leq 1$, and then keep trying until N are accepted. Here, f_{\max} is the largest value of $f(\mathbf{I})$, which is usually for a particle at rest in the center of the component.¹ There are many obvious, and some clever, means to improve efficiency, such as limiting $|\mathbf{x}| \leq r_{\max}$ and \mathbf{v} so that the candidate particle at the selected \mathbf{x} is gravitationally bound, *etc.*, but the vast majority of candidate particles are rejected because $f(\mathbf{I})$ is generally much smaller than its peak value over most of available phase space. Not only is this random sampling method inefficient, but it results in a distribution of \mathbf{I} values that differs by shot noise from the desired $f(\mathbf{I})$. While shot noise declines as $N^{-1/2}$, the benefit from increasing N is painfully slow.

Random sampling works because f specifies the mass in a $2n$ -dimensional volume element of Cartesian phase space $d^n \mathbf{x} d^n \mathbf{v}$ and generating candidate particles that are uniformly distributed in (\mathbf{x}, \mathbf{v}) space leads naturally to the probability of acceptance. We could choose candidate particles in some other system of coordinates, such as a set of integrals $\{\mathbf{I}\}$, which requires knowledge of the mass fraction, $d^m \mathcal{M}/d\mathbf{I}^m$ in an m -dimensional volume element of those integrals. This function is related to the mass in a Cartesian volume element through the Jacobian determinant of the coordinate trans-

¹ The referee pointed out that f_{\max} can be infinite in rare cases, although it must be an integrable singularity, since the mass within any small volume should be finite. However, random selection can still be achieved by transformation of variables, such as we describe in §2.

* E-mail: sellwood@as.arizona.edu

form, and some examples for different models are presented below. (Note that the density in action-angle coordinates is the same as in Cartesians, because the transformation between the two systems is canonical, but those variables suffer from the disadvantage that we generally do not have simple or exact algebraic expressions for them.) An important advantage, though not the only one, of this approach is that the dimensionality of the space of the variables \mathbf{I} is typically half, or less, that of phase space, because we can neglect, at least while we select the integrals, the corresponding phase angles, which must be uniformly populated in an equilibrium model.

However, if we were to select values for the integrals, \mathbf{I} , in the same random manner as the coordinates, (\mathbf{x}, \mathbf{v}) , the distribution of selected particles would still differ from the target DF by shot noise and we would have gained little. But the lower dimensionality of integral space makes it possible to select values deterministically in a smooth manner. With knowledge of the mass in an element of integral space, $d^m \mathcal{M}/d\mathbf{I}^m$, we can divide the space of the integrals into small boxes such that the size of each box $\Delta^m \mathbf{I}$ contains the mass fraction \mathcal{M}/N . Then choosing $\{\mathbf{I}\}$ values for a single particle in each such box ensures that selected particles have a density in the space of the integrals that is as close as possible, for the finite number of particles, to $f(\mathbf{I})$.

Rather than continue to discuss the general case, it is probably easier to convey the principle of the technique in a few simple examples, and we begin with the case of a razor-thin disk. Some extra effort is required to write the code to select a smooth distribution of integrals, but the running time to generate a given number of particles is comparable, or sometimes shorter, than even an optimized random sampling method.

There are two distinct strategies to limit Poisson noise. §2 describes the first, which is to reduce sampling errors in the selection of particles from the DF. The second is the much simpler strategy of imposing near axial symmetry, which we outline in §3. While axial symmetry results in a dramatic improvement, the more modest benefits of investing the extra effort in the selection of particles is still worthwhile. Note, they are two independent techniques that can be employed separately, as we illustrate in §4.

2 REDUCTION OF SAMPLING ERROR

The selection of particles in multi-component models should be made one component at a time. We here provide a detailed description of the technique, which may seem labored, in order that every step is clear.

2.1 A 2D disk with $f(E, L_z)$

Following Kalnajs (1976), we write the disk surface density as

$$\Sigma(R) = 2 \int_{v_R=0}^{\max} \int_{v_\phi=0}^{\max} f(v_R, v_\phi) \Big|_R dv_\phi dv_R, \quad (1)$$

where the factor 2 arises from having omitted inwardly moving stars from the outer integral. Also retrograde stars are generally omitted from the DF in rotationally-supported disks, but the equilibrium is unaffected if the sign of v_ϕ is

later reversed for some, which is desirable in order to smooth an unphysical discontinuity in the DF at $v_\phi = 0$.

We assume an axisymmetric potential $\Phi(R)$, so that $v_\phi = L_z/R$ and $E = \Phi(R) + \frac{1}{2}(v_R^2 + L_z^2/R^2)$, which we rearrange to obtain $v_R = [2(E - \Phi) - (L_z/R)^2]^{1/2}$, and change variables from (v_R, v_ϕ) to (E, L_z)

$$\Sigma(R) = 2 \int \int \frac{\partial(v_R, v_\phi)}{\partial(E, L_z)} f(E, L_z) dL_z dE. \quad (2)$$

The determinant of the Jacobian matrix is

$$\frac{\partial(v_R, v_\phi)}{\partial(E, L_z)} = \begin{vmatrix} 1/v_R & 0 \\ -L_z/(R^2 v_R) & 1/R \end{vmatrix} = \frac{1}{Rv_R}. \quad (3)$$

We therefore find

$$\Sigma(R) = 2 \int_{\Phi(R)}^0 \int_0^{R\{2[E-\Phi(R)]\}^{1/2}} \frac{f(E, L_z)}{Rv_R} dL_z dE, \quad (4)$$

where the upper limit on the inner integral is L_z of a circular orbit at radius R .

The total mass of the axisymmetric disk is

$$\begin{aligned} \mathcal{M} &= 2\pi \int_0^\infty R \Sigma(R) dR \\ &= 4\pi \int_0^\infty \int_{\Phi(R)}^0 \int_0^{R\{2[E-\Phi(R)]\}^{1/2}} \frac{f(E, L_z)}{v_R} dL_z dE dR. \end{aligned} \quad (5)$$

Interchanging the order of integration, we obtain

$$\mathcal{M} = 4\pi \int_{\Phi(0)}^0 \int_0^{L_{z,\max}(E)} \left\{ \int_{R_{\text{peri}}}^{R_{\text{apo}}} \frac{dR}{v_R} \right\} f(E, L_z) dL_z dE, \quad (6)$$

where R_{peri} and R_{apo} are respectively the radii of the inner and outer roots of $[2(E - \Phi) - L_z^2/R^2]^{1/2} = 0$, where the radial velocity changes sign, and $L_{z,\max}(E)$ is the angular momentum of a circular orbit of energy E . Note that f is independent of R , so the inner integral in braces, which is over outwardly moving stars only (eq. 1), is

$$\int_{R_{\text{peri}}}^{R_{\text{apo}}} \frac{dR}{v_R} = \frac{\tau(E, L_z)}{2}, \quad (7)$$

where τ is the full radial oscillation period for a particle in the adopted total potential. On differentiating the expression for \mathcal{M} , we obtain the mass in an infinitesimal element of (E, L_z) space:

$$\frac{d^2 \mathcal{M}}{dE dL_z} = 2\pi \tau(E, L_z) f(E, L_z). \quad (8)$$

2.1.1 Slicing by integrals

We use this last equation to slice (E, L_z) space into finite elements. The mass as a function of E is

$$M(E) = \int_{\Phi(0)}^E m_E(L_{z,\max}) dE, \quad (9)$$

with

$$m_E(L_z) = 2\pi \int_0^{L_z} \tau(E, L_z) f(E, L_z) dL_z. \quad (10)$$

The functions $m_E(L_z)$ and $M(E)$ are known only numerically, in general potentials, but they are monotonically increasing functions of their arguments since both f and τ are

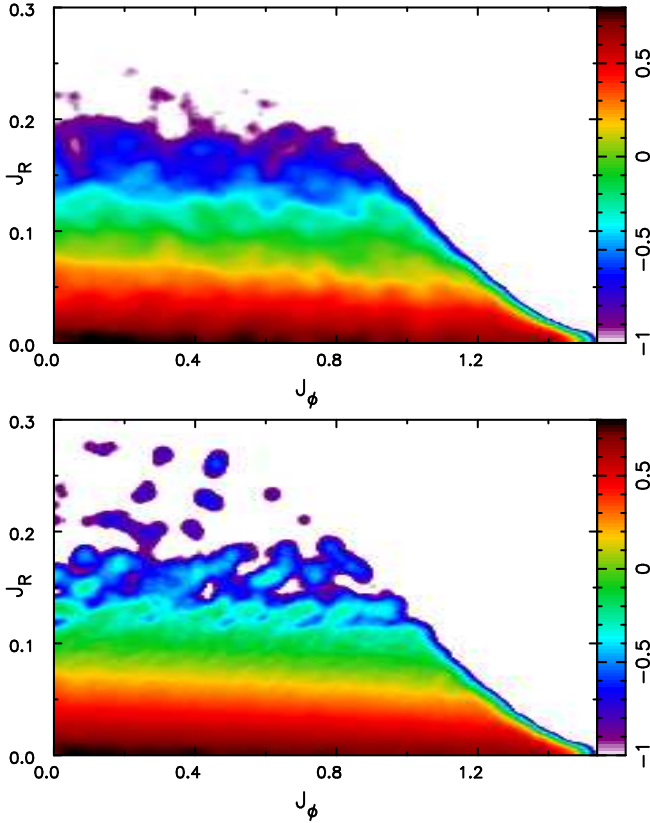


Figure 1. The logarithmic density of selected particles in the space of the two actions $J_\phi \equiv L_z$ and the radial action J_R when random sampling is used (upper panel) and when E and L_z are selected smoothly, as described here. 40K particles were selected by each method from the isochrone/12 DF described in §4.1, having no active particles outside $R = 4$. The sloping boundary at high L_z is caused by eliminating particles having enough energy to cross that radius. Notice the non-smoothness in the densely populated lower part of the upper panel.

positive. Thus we can determine the values $E(i_E)$ that divide \mathcal{M} into j_E equal pieces, $\delta M(E) = \mathcal{M}/j_E$, as can the values $L_{z,E}(i_L)$ that divide $\delta M(E)$ into j_L equal pieces. The mass enclosed in the rectangle bounded by $E(i_E)$ and $E(i_E + 1)$ and $L_{z,E}(i_L)$ and $L_{z,E}(i_L + 1)$ is $\mathcal{M}/(j_E j_L)$. If we were to choose just one particle to have (E, L_z) values that lie in this rectangle, we would reduce the sampling error of the function $f(E, L_z)$ to the minimum possible for the finite number, $j_E j_L$, of particles.

Since the product $j_E j_L$ is large, the variation of $f(\mathbf{I})$ over this small volume $\Delta^m \mathbf{I}$ is generally small and we select values for the integrals (E, L_z) to be those at a randomly chosen point within each mass element, which adds a little random noise to our careful sampling technique. The reasons for a random selection are that it is probably not a good idea for the selected particles to lie in a regular lattice in integral space and, perhaps more importantly, that $f(E, L_z)$ rises steeply in disks as $L_z \rightarrow L_{z,\max}(E)$, and choosing the center of every box, say, would introduce a bias against closely circular orbits.

The benefit of smooth selection is illustrated in Fig. 1, where the density of selected particles in the densely populated region at small J_R is smoother in the lower panel than

when random sampling is used (upper panel). These non-uniformities resulting from random sampling contribute to the evolution, and effectively create a different DF whose dynamical properties diverge from that of the intended smooth case.

2.1.2 Unequal mass particles

The total number of particles in a component is $N = j_E j_L j_R j_\phi$, with j_R and j_ϕ defined below. If all particles have equal mass, each has the mass \mathcal{M}/N .

However, it is sometimes useful to employ particles having a range of masses in order to concentrate more low mass particles in some part of integral space, which can readily be accomplished by this technique. The relative particle masses can be varied as the weight function $w(E, L_z)$, which must be positive over the entire range of these integrals, and which should be divided into eq. (6) to yield a pseudo-total mass

$$\mathcal{M}' = 2\pi \int_{\Phi(0)}^0 \int_0^{L_{z,\max}(E)} \frac{\tau(E, L_z) f(E, L_z)}{w(E, L_z)} dL_z dE. \quad (11)$$

We also divide the integrand in eq. (10) by the function $w(E, L_z)$ in order to make the appropriate changes to the values of $E(i_E)$ and $L_{z,E}(i_L)$ that slice up \mathcal{M}' . Then the mass of each of the $j_R j_\phi$ particles that have these revised integrals is $w(E, L_z) \mathcal{M}'/N$. Note that because of this factorization, there is no need to normalize the function $w(E, L_z)$.

The same idea can be applied to particle selection for non-disk components discussed in this section.

2.1.3 Selecting coordinates

Having selected the integrals, E and L_z , which define an orbit in the potential of the adopted model, we then need to choose positions and velocities. Integrating the orbit of the selected (E, L_z) for half a radial period in the adopted potential determines the time ($\propto v_R^{-1}$) a particle would spend at each radius. We select j_R values of R at random from uniform fractions *in time* of the orbit half-period. (I have experimented with spacing these radii at equal time intervals in order to further reduce jitter in the radial mass profile, but with no detectable improvement in practice.)

For each R , we have $v_\phi = L_z/R$, and $v_R = \pm[2(E - \Phi) - L_z^2/R^2]^{1/2}$, with either sign having equal probability since the inward and outward motions are anti-symmetric. The last remaining coordinate to be determined is the azimuthal position ϕ , which can be chosen at random from a uniform distribution, in which case $j_\phi = 1$. If $j_\phi > 1$, we can place copies of the particle each having coordinates (R, v_R, v_ϕ) at different azimuths ϕ , and substantially reduce the effects of shot noise by spacing them regularly in ϕ for a quiet start (Sellwood 1983; Sellwood & Athanassoula 1986), which is described in detail in §3.

Random selection of azimuthal phases really does introduce shot noise into the initial density distribution, that may be readily suppressed by imposing initial axial symmetry. But we also randomly select the radial phase and introduce a small random element in the selection of (E, L_z) values, which indeed re-introduces some noise and may seem to negate all the advantages gained in the effort to make a smooth selection of integral values. We address this point in §4.1.

2.2 A thickened disk

DFs that are functions of E and L_z only are unsuitable for thickened disks because the velocity dispersions in the radial and vertical directions are equal (Sellwood 2014b, eq. 13), making the disk unrealistically thick. However, we are generally unable to construct DFs that are functions of three integrals, $f(E, L_z, I_3)$ for at least two compelling reasons. First, we do not have a simple expression for I_3 , aside from numerical approximations (Binney 2010) and, second, parts of phase space can be chaotic. Despite this, Vasiliev (2019) provides two approximate DFs for thickened disks that are functions of 3 actions.

A more general and workable approximate method to construct an equilibrium for a 3D disk is to employ a 2D equilibrium model for a thin disk and treat the vertical motion as a separate 1D problem. We integrate the vertical 1D Jeans equation (Binney & Tremaine 2008, eq. 422b) for a slab, *i.e.* neglecting radial variations. In this case

$$\sigma_z^2(R, z) = \frac{1}{\rho(R, z)} \int_z^\infty \rho(R, z') \frac{\partial \Phi}{\partial z} dz', \quad (12)$$

where the vertical gradient of the total potential Φ should be determined from the disk itself, as well as any additional mass components. This formula generally yields an acceptable equilibrium when the radial excursions of disk particles are small, but when this is not the case, the disk adjusts quickly to a mild imbalance because the vertical oscillation period is short – see §4.3 for an example. The method is versatile because it allows any reasonable vertical density profile $\rho(R, z)$, and works in the presence of other mass components that contribute to the total potential.

Sanders & Binney (2016) reviewed this and other methods to construct a thickened disk, and found that methods based on a Stäckel approximation are superior and yield a better disk equilibrium. We report in §4.3 that the initial model we use there is slightly out of balance, and a better method would be desirable, especially for disks that might be hotter or thicker than that we employed.

2.3 A spherical model with $f(E, L)$

A sphere of stars that has an anisotropic velocity distribution, requires a DF that is a function of both E and the total angular momentum L . The velocity dispersion tensor must everywhere be aligned with the radius vector, else the mass distribution will be aspherical. Since all orbits are planar, the velocity at each point has just two components, v_r and v_\perp , and the v_\perp directions of all orbits passing through any point are uniformly distributed in a circularly symmetric fashion about the radius vector. Thus we have

$$\rho(r) = \int f(v_r, v_\perp) \Big|_r d^3 \mathbf{v} = \int \int 2\pi v_\perp f(v_r, v_\perp) \Big|_r dv_\perp dv_r, \quad (13)$$

where the $2\pi v_\perp$ factor arises from integrating out the uniform directional distribution of v_\perp . As usual, $L = rv_\perp$ and $E = \Phi(r) + \frac{1}{2}(v_r^2 + v_\perp^2)$, so $v_r = [2(E - \Phi) - (L/r)^2]^{1/2}$.

Changing variables from (v_r, v_\perp) to (E, L) , we have

$$\rho(r) = 4\pi \int \int \frac{\partial(v_r, v_\perp)}{\partial(E, L)} v_\perp f(E, L) dL dE, \quad (14)$$

where the integral is doubled, as for the disk, to take account

of both inwardly and outwardly moving stars. The determinant of the Jacobian matrix clearly is $1/(rv_r)$, since it differs from that in the disk simply by the substitution of v_\perp for v_ϕ , and we therefore find

$$\rho(r) = 4\pi \int \int \frac{v_\perp}{rv_r} f(E, L) dL dE. \quad (15)$$

The total mass of the sphere is therefore

$$\begin{aligned} \mathcal{M} &= 16\pi^2 \int_0^\infty r^2 \int_{\Phi(r)}^0 \int_0^{\max} \frac{v_\perp}{rv_r} f(E, L) dL dE dr \\ &= 8\pi^2 \int_{\Phi(0)}^0 \int_0^{L_{\max}(E)} L \tau(E, L) f(E, L) dL dE, \end{aligned} \quad (16)$$

where τ is the full radial oscillation period, as before. Thus the mass in an infinitesimal element of (E, L) space is

$$\frac{d^2 \mathcal{M}}{dE dL} = 8\pi^2 L \tau(E, L) f(E, L). \quad (17)$$

2.3.1 Particle selection

The procedure is very nearly the same as for the disk case described in §2.1 above. We use this last equation to slice (E, L) space into elements that each contain mass $\mathcal{M}/(j_E j_L)$, and then select values for the integrals of each particle (E, L) to be those at a randomly chosen point within each element. We again integrate the planar orbit of the selected (E, L) for half a radial period in the adopted spherical potential to determine the time a particle would spend at each radius, and we select j_r values of r (typically at random) from uniform fraction of the radial half-period. Having chosen r , we have $v_\perp = L/r$, and $v_r = \pm[2(E - \Phi) - L^2/r^2]^{1/2}$, again with either sign having equal probability.

In this case, we must also choose the orientation of the orbit plane, which is uniformly distributed in the cosine of the polar angle $-\pi/2 < \theta < \pi/2$, and which requires r to be resolved into (R, z) and v_r into components v_R and v_z . The last remaining coordinate to be determined is the azimuthal position ϕ – see §3.

2.4 An ergodic sphere model with $f(E)$

In this case, the velocity distribution is everywhere isotropic and we have $d\mathbf{v}^3 = 4\pi v^2 dv$. Thus

$$\rho(r) = 4\pi \int_0^{v_{\max}} f(E) v^2 dv, \quad (18)$$

where $v_{\max} = \{2[E - \Phi(r)]\}^{1/2}$. While $f(E)$ is independent of L , the radial period $\tau(E, L)$ is not, and it is therefore simplest to adopt the same procedure to select integrals (E, L) and particle coordinates as for the anisotropic, spherical case in §2.3 above, while keeping the DF uniform in L .

2.5 A spheroidal model with $f(E, L_z)$

For this case, we choose the z -axis as the axis of rotational symmetry, so that ρ and Φ are functions of both R and z . The velocity at any point is (v_ϕ, ψ, v_m) (Binney & Tremaine 2008, §4.4.1), with v_ϕ being perpendicular to the radius vector and lying in a plane at height z parallel to the symmetry

plane. The component v_m , lies in the meridional plane² and is uniformly distributed in the angle ψ such that $v_R = v_m \cos \psi$ and $v_z = v_m \sin \psi$. Therefore

$$\begin{aligned} \rho(R, z) &= \int f(\mathbf{x}, \mathbf{v}) v_m dv_m d\psi dv_\phi \\ &= 2\pi \int_0^{\sqrt{2(E-\Phi)}} \int_{-v_{\phi, \max}}^{v_{\phi, \max}} f v_m dv_\phi dv_m, \end{aligned} \quad (19)$$

since f does not depend on ψ , and $v_{\phi, \max} = [2(E - \Phi) - v_m^2]^{1/2}$. Note that $v_m \geq 0$ while v_ϕ can have either sign. Changing variables, the determinant of the Jacobian matrix, $\partial(v_m, v_\phi)/\partial(E, L_z) = (Rv_m)^{-1}$, and so we have

$$\rho(R, z) = 2\pi \int_{\Phi(R, z)}^{E_{\max}} \int_{-L_{z, \max}(E)}^{L_{z, \max}(E)} \frac{f(E, L_z)}{Rv_m} v_m dL_z dE, \quad (20)$$

where $L_{z, \max}(E) = R[2(E - \Phi)]^{1/2}$.

The mass of the spheroid is

$$\begin{aligned} \mathcal{M} &= 2\pi \int \int \rho(R, z) R dz dR \\ &= 4\pi^2 \int_0^\infty \int_{-z_{\max}(R)}^{z_{\max}(R)} \int_{\Phi(R, z)}^0 \int_{-L_{z, \max}(E)}^{L_{z, \max}(E)} \\ &\quad f(E, L_z) dL_z dE dz dR \\ &= 4\pi^2 \int_{\Phi(0, 0)}^0 \int_{-L_{z, \max}(E)}^{L_{z, \max}(E)} \left\{ \int_{\text{peri}}^{\text{apo}} \int_{-z_{\max}(R)}^{z_{\max}(R)} dz dR \right\} \\ &\quad f(E, L_z) dL_z dE. \end{aligned} \quad (21)$$

Note that the boundary of the double integral within the braces is the zero velocity curve in the meridional plane of an orbit having integrals (E, L_z) and, since the integrand is unity within that boundary, the double integral is simply the area $S(E, L_z)$ bounded by the zero-velocity curve. Thus the mass in an infinitesimal element of (E, L_z) space is

$$\frac{d^2 \mathcal{M}}{dE dL_z} = 4\pi^2 S(E, L_z) f(E, L_z). \quad (22)$$

Once again, we use this last equation to slice (E, L_z) space into elements that each contain mass $\mathcal{M}/j_E j_L$, and then select values for the integrals (E, L_z) to be those at a randomly chosen point within each element. Since the area S in the meridional plane is uniformly populated, we choose j_R values of both R and z at random from within that area. The selected radii determine $v_\phi = L_z/R$ and $v_m = \{2[E - \Phi(R, z)] - L_z^2/R^2\}^{1/2}$ (strictly positive this time). The velocity v_m is oriented at random in the meridional plane so we choose $0 < \psi < 2\pi$, from which v_R and v_z follow. As always, it remains only to choose the azimuth ϕ .

3 AZIMUTHAL SYMMETRY

If the azimuthal coordinates ϕ were selected at random, then non-axisymmetric forces would be subject to the full level of

² A plane containing the star that rotates about the symmetry axis, at the time-varying rate $\dot{\phi} = L_z/R$. The Cartesian position of the star within the plane at any instant is (R, z) .

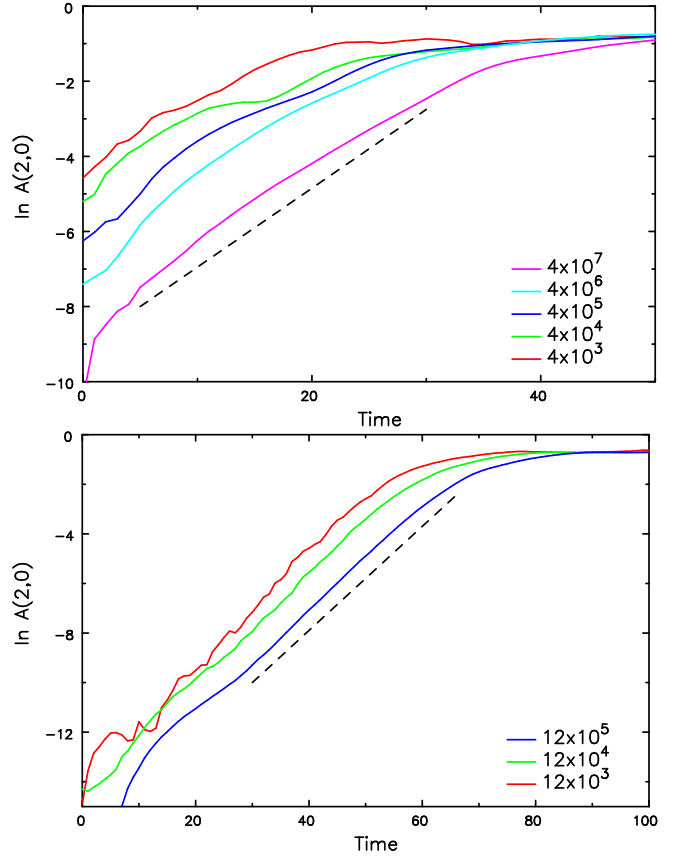


Figure 2. Upper: The growth of a bisymmetric disturbance in an unstable disk in five simulations having differing numbers of particles. The unstable disk model and the simulation method are described in §4.1 and all began with the particles placed at random azimuths. The dashed line indicates the expected growth rate of the dominant instability. Lower: As for the upper panel, but for three simulations that began with two additional replica particles placed evenly around rings for each case. Note the changes of scale to both axes.

shot noise expected from N particles. In an unstable model, the seed amplitude of a non-axisymmetric instability would be high, unless N were extremely large, and by the time linear growth causes the unstable mode to emerge from the noise it may be already be close to the saturation amplitude, making any estimate of the rate of growth of the instability highly uncertain. This behavior is illustrated in the upper panel of Fig. 2, which reports the growth of a bisymmetric disturbance in the unstable disk model described in §4.1. The curves indicate very gradual progress towards the expected result as N is increased; in particular, there was no period of exactly exponential growth even when 40 million particles were employed.

However, Sellwood (1983) demonstrated that we can substantially reduce the seed amplitude of all low-order non-axisymmetric instabilities by employing the simple strategy of placing j_ϕ particles, each having the same radius and velocity components in polar coordinates, at equal intervals in $\Delta\phi = 2\pi/(m_{\text{sect}} j_\phi)$ around an arc of a circle, and starting from a randomly chosen initial phase $0 < \phi_0 < \Delta\phi$ for each ring. In this formula, if m_{sect} is the only active sectoral har-

monic,³ Fourier synthesis in azimuth replicates the particles in other sectors. The dramatic improvement that results from this simple change is shown in the lower panel of Fig. 2 that reveals approximately exponential growth by a much larger factor that closely tracks the predicted linear growth rate, and is not a bad match even for the smallest N shown!

The minimum number of particles required per ring on the polar grid is not quite trivial. As ring particles are driven away from perfect symmetry by a growing disturbance, their displacements must be prevented from contributing, through aliases, to other force terms, which requires the number of equally spaced particles in an arc of $2\pi/m_{\text{sect}}$ to be at least $j_\phi = (2m_{\text{max}} + 1)/m_{\text{sect}} + 1$. Here m_{max} is the highest active sectoral harmonic, which could be a multiple of m_{sect} . In more general methods, in which force terms are not restricted to a few low-order sectoral harmonics, the effective value of $m_{\text{sect}} = 1$, and j_ϕ should be larger. For a 3D axisymmetric model, j_ϕ should be doubled, since all particles on one ring should have the same z distance from the mid-plane and be reproduced in a reflection symmetric ring, in which both z and v_z have the opposite signs. In practice, we give each of the j_ϕ particles a small, typically $\lesssim 0.1^\circ$, random nudge in azimuth to create a seed disturbance.

This procedure suppresses shot noise in the low-order terms of the density distribution, at the expense of a greatly enhanced signal from the sectoral harmonic of the imposed rotational symmetry, $m = j_\phi/(n_{\text{dim}} - 1)$ where $n_{\text{dim}} = 2$ or 3 , and its multiples. With a polar grid, it is straightforward to suppress forces from this artificially boosted non-axisymmetric term, but with more general force methods, the response to the strongly enhanced amplitude of a sectoral harmonic having $m = j_\phi$ should be mild provided j_ϕ is large, say $j_\phi \gtrsim 20$ – see §3.4 of Sellwood & Carlberg (2023) for a successful example using a Cartesian grid.

Note that the purpose of imposing initial axial symmetry is to *hide* the particulate nature of the model. Since the gravitational field is that of a smooth mass distribution, each of the j_ϕ particles pursues a congruent orbit, maintaining the initially symmetric arrangement. Thus the particles on each ring mimic a circular wire of uniform mass per unit length that oscillates radially. The rings distort smoothly as the particles respond to any developing low-order non-axisymmetric disturbances, and generally maintain coherence until the instability saturates. Note that the mutual gravitational attractions of particles are smoothed by restricting force terms to a few active sectoral harmonics, which almost eliminates the microscopic chaos that afflicts systems of point mass particles (*e.g.* Miller 1964; Kandrup & Smith 1991; Goodman, Heggie & Hut 1993; Hemsendorf & Merritt 2002).

The survival time of ring coherence depends upon the responsiveness of the dynamical model to density fluctuations, which is a particular problem in dynamically cool disks. The rings break up even in the absence of a global instability because the supporting response of the surrounding disk to even mild density inhomogeneities results in density wakes (Julian & Toomre 1966; Binney 2020) that further disturb the regular arrangement, leading to exponential growth of

noise. Fortunately, the growth rate of an unstable mode, when present, also depends upon the responsiveness of the disk (Sellwood & Masters 2022), and generally we find that the dominant instability outgrows the noise. Without a dominant instability, the growth of noise must cease when the rings have been completely randomized, and any subsequent evolution will be no different from that in a model started from random azimuths (*e.g.* Sellwood 2012).

As just mentioned, the use of a polar grid to determine the gravitational field has the further advantage that it is straightforward to restrict non-axisymmetric force terms acting on the particles to a single specified sectoral harmonic, m_{sect} . Note, however, that simulations in which disturbance forces are restricted to a single m_{sect} , do not capture the correct behavior once the instability saturates. As the amplitude approaches saturation, density variations develop at other sectoral harmonics, typically $m = 0$ and at low multiples of the originally active m_{sect} , that should contribute to the total self-consistent gravitational field if the simulation is meaningfully to be continued beyond linear growth.

4 SOME NUMERICAL RESULTS

We choose three distinct models to illustrate the advantages of the particle selection procedures described in §2. These models deliberately employ quite modest numbers of particles in order to demonstrate more clearly the advantages of smooth selection. Initial azimuthal symmetry (§3) was used in only the first example, while all three compare random sampling with smooth selection.

4.1 The linear mode of the isochrone disk

The improved behavior resulting from these techniques is apparent from measurements of the frequency of a global instability. Our chosen example is the 2D isochrone disk (Binney & Tremaine 2008, §2.2.2(d)), for which Kalnajs (1976) derived a family of DFs. The full-mass isochrone/12 disk has $Q \simeq 1.1$ over the inner disk and Kalnajs (1978) used a matrix method to predict the frequency of the dominant unstable mode. We computed disturbance forces from the particles by a basis function method (Earn & Sellwood 1995; Sellwood 2014a), employing $m = 2$ terms only, while adding at every step the central attraction of the disk to the self-consistent disturbance force on each particle. In two separate sets of simulations, we selected 40K particles from the DF by random sampling in one set and by smooth sampling (§2.1) in the other set, using a different random seed for each case. For both sets, we imposed initial axial symmetry (§3) with $j_\phi = 3$ particles spaced evenly around a half-circle (making $N = 120\text{K}$ total) and ran each simulation until the instability saturated. The advantage of imposing axial symmetry was already illustrated in Fig. 2, while here we show that smooth selection of particles yields a further, but less dramatic improvement.

As usual, we measure the instantaneous amplitude of bi-symmetric disturbances in the distribution of the N particles using an expansion in logarithmic spirals:

$$A(m, \gamma, t) = \frac{1}{N} \sum_{j=1}^N \exp[im(\phi_j + \tan \gamma \ln R_j)], \quad (23)$$

³ this author's preferred term and that of Lindblad (1963, and references therein) but aka angular harmonic

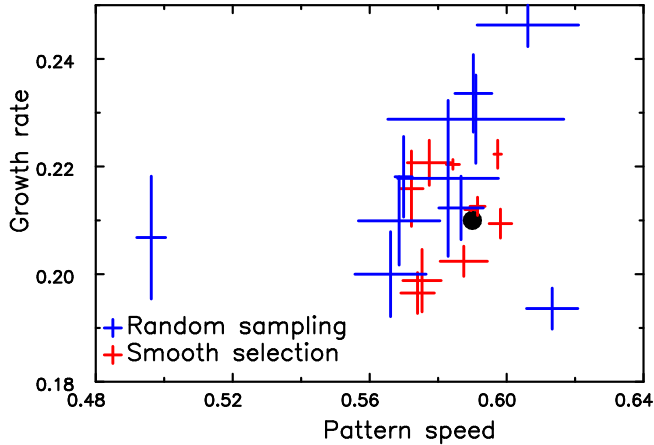


Figure 3. The scatter from many simulations of the measured pattern speed and growth rate of the dominant mode of the isochrone/12 disk. Each colored point is the best-fit value from a simulation employing 120K particles, with error bars indicating the full range from different acceptable fits to the data. The blue points record the measured values when random sampling is used, the red points when the sampling error is reduced by the smooth selection procedure described in §2.1. The large black dot marks the frequency predicted by Kalnajs (1978) from linear theory.

where, $m = 2$, (R_j, ϕ_j) are the polar coordinates of the j th particle at time t , and γ is the (radially constant) angle of the spiral component to the radius vector, which is the complement to the spiral pitch angle. We estimated the linear frequency of the dominant mode from fits to these measurements, and to the coefficients of the basis expansion by the method described by (Sellwood & Athanassoula 1986).

Figure 3 presents the estimated frequency, with error bars, of the dominant instability in each of multiple simulations having a different random seed. The frequency predicted from linear theory by Kalnajs (1978) is marked by the black dot. The blue points report the estimated eigenfrequency in separate simulations in which coordinates of the independent particles were selected by random sampling, while the red points show the values from a separate set of simulations in which the integrals for the particles were selected in the smooth manner described in §2.1. The blue symbols range $\pm 21\%$ (or $\pm 8\%$ if the outlier is omitted) from the mean pattern speed and $\pm 24\%$ from the mean value of the growth rate, whereas the ranges of the red symbols are respectively $\pm 4.4\%$ and $\pm 12\%$.

Thus it seems that noise in the distribution of (E, L_z) values (Fig. 1) causes a larger spread in the measured frequencies than we obtained from a smooth distribution, though the difference is not spectacular. Differences in the measured frequencies arise, for the most part, because the unstable mode in each simulation is not that of the intended model, but of one having a DF that differs by shot noise.

The error bars, and the scatter of the points, from both methods diminish as the number of particles is increased, and indeed Earn & Sellwood (1995) were able to obtain excellent agreement with the predicted value from larger simulations.

Figure 3 also demonstrates that random selection the sub-box values of (E, L_z) and of radial phases described in §2.1 does not, in practice, re-establish full shot noise, since the spread of the red points is smaller than that of the blue.

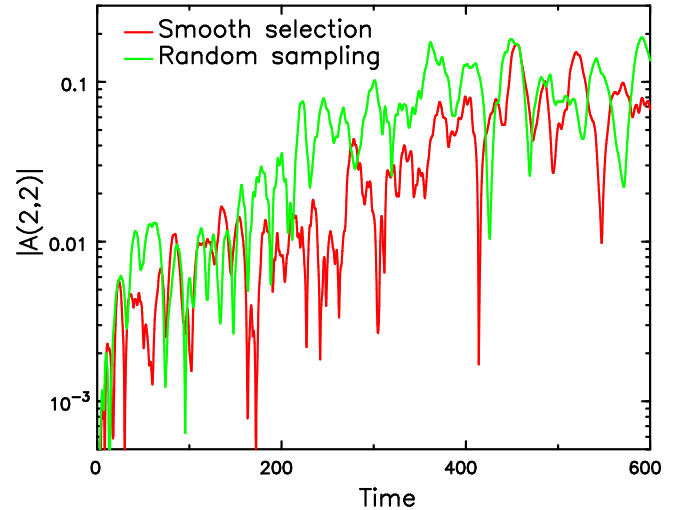


Figure 4. The time evolution of the amplitude of a logarithmic spiral component in two simulations of a linearly-stable, half-mass Mestel disk. Both had $N = 5M$ particles, the same grid parameters, softening length, and time step. Notice that the secular rise in amplitude is a little more rapid when the initial particles were selected by random sampling.

4.2 The rise of amplified noise in the Mestel disk

Toomre (1981) had predicted that the half-mass Mestel disk, which has a constant circular speed V_0 at all radii, was linearly stable. However, simulations of this model reported by Sellwood (2012) found that swing-amplified particle noise, even with $N = 5 \times 10^8$ particles, created “scratches” in the DF as each non-axisymmetric disturbance was absorbed through non-linear scattering at its inner Lindblad resonance (ILR). The modified DF then supported larger amplitude disturbances that in turn created deeper scratches, causing secular growth until the grooves in the DF were pronounced enough to seed a linear instability that created a strong bar. Sellwood (2012) selected particles for all his simulations by the smooth method described in §2.1, and here we show that a model in which random sampling of particles was employed caused secular growth of non-axisymmetric features to occur more rapidly.

We again use the 2D polar grid that Sellwood (2012) employed, with disturbance forces restricted to $m = 2$ and, as for the isochrone disk above, we added the central attraction to each particle at each step. We compare the evolution of two simulations having $N = 5M$ that employed either smooth selection or random sampling from the DF, with the initial azimuthal coordinates selected at random (*i.e.*, $j_\phi = 1$). The unit of time is R_0/V_0 , where R_0 is the mean radius of the central cutout; see Sellwood (2012) for details of the DF, and the inner and outer tapers to the otherwise cusped and infinite disk.

Figure 4 presents the time evolution of the $m = 2$, $\tan \gamma = 2$ component in both simulations. As Sellwood (2012) reported, the amplitude starts out by rising quite rapidly as the particle distribution becomes polarized, and the time evolution in both models is characterized by rapid fluctuations due to interference between swing-amplified transients having different corotation radii in the disk. Note, we stopped these simulations at $t = 600$, while the $N = 5M$ simulation in

that earlier paper was continued to $t = 1500$ with no significant amplitude changes during the second half of the evolution. Note that here we report the amplitude of a logarithmic spiral component, whereas [Sellwood \(2012\)](#) chose a different measure.

However, the secular rise of the amplitude in the model that began from randomly sampled particles is more rapid than that in which particles were selected more carefully. The only difference between these two cases is that values of the integrals E and L_z differ by shot noise from those in the analytic DF when random sampling is used, whereas that part of the shot noise is strongly suppressed with smooth selection. The more rapid secular growth is probably caused by mild instabilities triggered by the non-uniformities in the density of particles as a function of the integrals, of the kind illustrated in the upper panel of [Fig. 1](#).

4.3 A disk-halo model

As the first model addressed an instability of an isolated disk and the second a disk embedded in a rigid halo, we here add a slightly more realistic example of an axisymmetric exponential disk embedded in a halo of live particles. The disk surface density profile is

$$\Sigma(R) = \frac{M_d}{2\pi R_d^2} e^{-R/R_d}, \quad (24)$$

where R_d is the disk scale length and M_d is the nominal mass of the infinite disk. We limit its radial extent using a cubic function to taper the surface density smoothly from $\Sigma(4.5R_d)$ to zero at $R = 5R_d$.

The halo is an originally isotropic Hernquist sphere ([Hernquist 1990](#)) which has been compressed adiabatically ([Sellwood & McGaugh 2005](#)) by the addition of the disk mass at its center. The original halo had a nominal mass of $80M_d$ and a core radius of $30R_d$, and its infinite extent was restricted by eliminating all particles having sufficient energy, before compression, to pass $r = 70R_d$, creating a smooth decrease in density to zero at that radius. We compress the halo using the grid-determined, softened field of the thickened and truncated disk, using the radial attraction in the disk mid-plane, which we adopt as spherically symmetric. Since both the angular momentum and radial action are conserved during compression, the compressed $f_c(E, L)$, which becomes anisotropic, has the same value for the two actions J_r and J_ϕ ([Young 1980](#); [Sellwood & McGaugh 2005](#)) as the original $f_H(E)$ given in Hernquist’s paper.

Once the combined potential, $\Phi(R, z)$, of the disk and compressed halo is known, we can solve for the DF of the disk, using the method proposed by [Shu \(1969\)](#). The in-plane DF has the form

$$f(E, L_z) = \begin{cases} \mathcal{F}(L_z) e^{-\mathcal{E}/\sigma_R^2(R_g)} & 0 < \mathcal{E} \leq -E_c(L_z), \\ 0 & L_z < 0. \end{cases} \quad (25)$$

Here \mathcal{E} is the excess energy of a particle above E_c , which is that of a circular orbit at the guiding center radius $R_g(L_z)$. Although this DF assumes no retrograde stars, we later reverse the angular momentum of some low- L_z particles in order to smooth the discontinuity in $f(E, L_z)$ at $L_z = 0$, which does not affect the equilibrium. The DF (25) clearly assumes a Gaussian radial velocity distribution everywhere, but the azimuthal velocity distribution is appropriately skewed. We

Table 1. Numerical parameters of the disk-halo simulations

Cylindrical polar grid	
Mesh points in (r, ϕ, z)	$127 \times 192 \times 125$
Spacing of planes	$R_d/50$
Active sectoral harmonics	$m = 0$ only
Spline softening length	$\epsilon = R_d/20$
Spherical grid	
Outer boundary	$r_{\max} = 80R_d$
Radial shells	501
Active surface harmonics	$l = 0$ only
Grid scaling	$R_d = 10$ grid units
Number of disk particles	2×10^5
Number of halo particles	2×10^5
Shortest and longest time-step	$\tau_{\text{dyn}}/80$ and $\tau_{\text{dyn}}/5$
Radial time step zones	5

set the radial velocity dispersion of the disk particles using the [Toomre \(1964\)](#) criterion $\sigma_R(R) = Q \cdot 3.36G\Sigma/\kappa$, where κ is the local epicyclic frequency ([Binney & Tremaine 2008](#)), choosing $Q = 1.5$ at all radii.

The function $\mathcal{F}(L_z)$ has to be determined numerically and the procedure we adopt is described in the on-line manual ([Sellwood 2014a](#)). As there are many possible functions \mathcal{F} that fit the adopted disk surface density and Q profile, we impose two extra requirements. Not only are rapid fluctuations of \mathcal{F} with L_z physically unreasonable, but we have also found that even mild “ripples” in the function $\mathcal{F}(L_z)$ can seed disk instabilities related to groove modes ([Sellwood & Masters 2022](#)). We therefore penalize the fit to the surface density also to minimize $T = \sum_{L_z} [d^2\mathcal{F}/dL_z^2]^2$. Note that the numerical search for the optimum \mathcal{F} seeks a balance between fitting the disk surface density while also minimizing T , and finding the optimum balance is something of an art. It is also required that $\mathcal{F}(L_z) \geq 0$ for all L_z , although we find that this requirement is generally satisfied for a smooth \mathcal{F} without imposing an additional constraint.

The disk particles are distributed vertically in a Gaussian distribution having a spread $z_0 = 0.1R_d$ at all radii and their vertical velocities are set using eq. (12).

Here we use units such that $G = M_d = R_d = 1$. Our unit of time is therefore $\tau_{\text{dyn}} = (R_d^3/GM_d)^{1/2}$. For those who prefer physical units, a possible scaling is to set $R_d = 2$ kpc, and $\tau_{\text{dyn}} = 10$ Myr, which implies $V_0 \simeq 176$ km s⁻¹ and $M_d \simeq 1.78 \times 10^{10} M_\odot$.

We compute the evolution of the model using a hybrid grid method, see [Sellwood \(2014a\)](#) for a full description. The evolution of the disk particles is computed using a 3D cylindrical polar grid, while accelerations of the halo particles are computed through a spherical grid; naturally, all particles experience forces from those of both components at every step. The numerical parameters adopted are given in [Table 1](#).

[Figure 5](#) reports the evolution of the virial ratio, $T/|W_C|$, over a short time interval of $80\tau_{\text{dyn}}$, or about three orbit periods at $R = 3R_d$, in a number of simulations. The virial of Clausius $W_C = \sum_N \mu_i \mathbf{a}_i \cdot \mathbf{x}_i$, with μ_i , \mathbf{a}_i , and \mathbf{x}_i being respectively the mass, acceleration, and position of the i th particle at the given moment. The model is very slightly out of balance initially, as $T/|W_C| \sim 0.506$ (note the small range of the vertical scale), but settles within $\sim 20\tau_{\text{dyn}}$ as the disk adjusts to its very mild disequilibrium caused by the imperfection of eq. (12).

The solid black line reports the case in which particles were

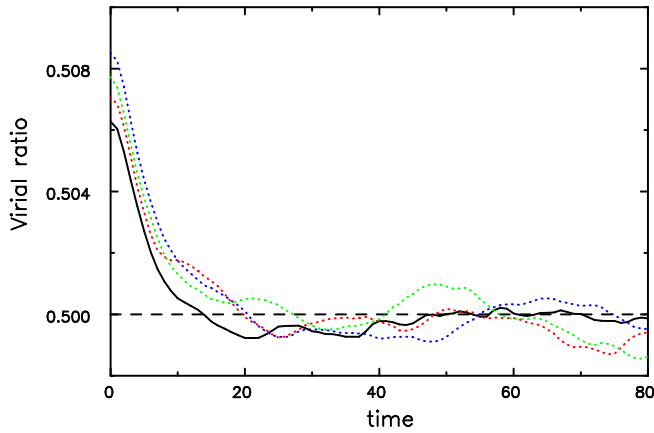


Figure 5. The evolution of the virial ratio of multiple realizations of the model described in §4.3. The solid black line is for a simulation in which both the disk and halo particles were selected in the smooth manner described respectively in §§2.1 & 2.5. The colored dotted curves are from simulations in which the initial coordinates of both components were chosen by random sampling, using a different random seed in each case. The very slight initial disequilibrium, reflected by the initial drop, is caused by the vertical adjustment of the disk thickness, because of the approximate set up using eq. (12). All four simulations were forced to remain axisymmetric for this test to prevent the development of a bar, which would otherwise begin to emerge by $t \sim 30$.

selected from the DFs for both the disk and halo using the smooth methods described in §2, and the colored dotted lines are from models that used random sampling, each having a different random seed. Since the virial ratio is affected in later evolution by a growing bar instability in this disk-halo model, we suppress all non-axisymmetric force terms in order that the model simply settles to an axisymmetric equilibrium. It can be seen from this Figure that random sampling not only introduces differences in the initial virial ratio, but causes persisting fluctuations that reflect mild collective changes from noise-driven evolution. However, the differences are minor.

5 CONCLUSIONS

In order to construct a simulation that is initially in equilibrium, it is best to select particle coordinates from a distribution function (DF). Having invested effort to create an equilibrium DF, it makes sense also to try to minimize the sampling error when selecting particles from it. We have presented methods that can be used to reduce sampling noise in the selection of particles and, though they require extra effort to program, they do not take significantly more cpu time to run than does the random sampling approach that is widely used. With random sampling, initial noise can also be reduced, albeit slowly, by increasing the number of particles, but methods that yield a similar improvement without increasing N have clear practical advantages.

We have presented three sets of models to illustrate the advantages of this approach. These simulations employ quite modest numbers of particles in order to illustrate the advantages more clearly. The frequency of an unstable mode is more reliably reproduced when particles are selected in a

smooth manner in the case examined in §4.1, while we show in §4.2 that non-axisymmetric disturbances grow slightly more rapidly in simulations of the stable Mestel disk when started from a randomly sampled set of particles. Finally, the models presented in §4.3 are slightly closer to equilibrium when smooth sampling is employed. The improvement in all three cases is clear, though not dramatic.

ACKNOWLEDGEMENTS

The ideas described here were developed over many years in collaborations with Lia Athanassoula, Victor Debattista, David Earn, Juntao Shen, and Monica Valluri, and I am eternally grateful for their assistance. I am especially indebted to Victor Debattista, who suggested I include the example of the Mestel disk presented in §4.2. An anonymous referee made a number of thoughtful suggestions to strengthen the paper. The author also acknowledges a helpful email discussion with James Binney and the continuing hospitality and support of Steward Observatory.

DATA AVAILABILITY

The data from the simulations reported here can be made available on request. The source code for particle selection, as well as the simulation and analysis software can be downloaded in one bundle from <http://www.physics.rutgers.edu/galaxy>, and is fully documented in the code manual (Sellwood 2014a).

REFERENCES

- Binney, J. 2010, *MNRAS*, **401**, 2318
 Binney, J. 2020, *MNRAS*, **496**, 767
 Binney, J. & Tremaine, S. 2008, *Galactic Dynamics* 2nd Ed. (Princeton: Princeton University Press)
 Debattista, V. P. & Sellwood, J. A. 2000, *ApJ*, **543**, 704
 Earn, D. J. D. & Sellwood, J. A. 1995, *ApJ*, **451**, 533
 Goodman, J., Heggie, D. C. & Hut, P. 1993, *ApJ*, **415**, 715
 Hemsendorf, M. & Merritt, D. 2002, *ApJ*, **580**, 606
 Hernquist, L. 1990, *ApJ*, **356**, 359
 Hernquist, L. 1993, *ApJS*, **86**, 389
 Holley-Bockelmann, K., Weinberg, M. & Katz, N. 2005, *MNRAS*, **363**, 991
 Julian, W. H. & Toomre, A. 1966, *ApJ*, **146**, 810
 Kalnajs, A. J. 1976, *ApJ*, **205**, 751
 Kalnajs, A. J. 1978, in *IAU Symposium 77 Structure and Properties of Nearby Galaxies* eds. E. M. Berkhuisjen & R. Wielebinski (Dordrecht:Reidel) p. 113
 Kandrup, H. E. & Smith, H. 1991, *ApJ*, **374**, 255
 Kuijken, K. & Dubinski, J. 1995, *MNRAS*, **277**, 1341
 Lindblad, B. 1963, *Stockholm Obs. Ann.*, **22**, No. 5
 Miller, R. H. 1964, *ApJ*, **140**, 250
 Rodionov, S. A., Athanassoula, E. & Sotnikova, N. Ya. 2009, *MNRAS*, **392**, 904
 Sanders, J. L. & Binney, J. 2016, *MNRAS*, **457**, 2107
 Sellwood, J. A. 1983, *J. Comp. Phys.*, **50**, 337
 Sellwood, J. A. 2012, *ApJ*, **751**, 44
 Sellwood, J. A. 2014a, arXiv:1406.6606 (on-line manual: <http://www.physics.rutgers.edu/~sellwood/manual.pdf>)
 Sellwood, J. A. 2014b, *Rev. Mod. Phys.*, **86**, 1
 Sellwood, J. A. & Athanassoula, E. 1986, *MNRAS*, **221**, 195

- Sellwood, J. A. & Carlberg, R. G. 2023, *ApJ*, **958**, 182
Sellwood, J. A. & Masters, K. L. 2022, *ARA&A*, **60**, 73
Sellwood, J. A. & McGaugh, S. S. 2005, *ApJ*, **634**, 70
Shu, F. H. 1969, *ApJ*, **158**, 505
Toomre, A. 1964, *ApJ*, **139**, 1217
Toomre, A. 1981, In *The Structure and Evolution of Normal Galaxies*, eds. S. M. Fall & D. Lynden-Bell (Cambridge, Cambridge Univ. Press) p. 111
Vasiliev, E. 2019, *MNRAS*, **482**, 1525
Widrow, L. M., Pym, B. & Dubinski, J. 2008, **679**, 1239
Young, P. 1980, *ApJ*, **242**, 1232
Yurin, D. & Springel, V. 2014, *MNRAS*, **444**, 62

This paper has been typeset from a $\text{\TeX}/\text{\LaTeX}$ file prepared by the author.